Angle resolved vibrational properties of anisotropic transition metal trichalcogenide nanosheets

Wilson Kong,[a] Cihan Bacaksiz,[b] Bin Chen,[a] Kedi Wu,[a] Mark Blei,[a] Xi Fan,[a] Yuxia Shen,[a] Hasan Sahin,[c] David Wright,[d] Deepa S. Narang[e] and Sefaattin Tongay*[a]

Layered transition metal trichalcogenides (TMTCs) are a new class of anisotropic two-dimensional materials that exhibit quasi-1D behavior. This property stems from their unique highly anisotropic crystal structure where vastly different material properties can be attained from different crystal directions. Here, we employ density functional theory predictions, atomic force microscopy, and angle-resolved Raman spectroscopy to investigate their fundamental vibrational properties which differ significantly from other 2D systems and to establish a method in identifying anisotropy direction of different types of TMTCs. We find that the intensity of certain Raman peaks of TiS_3, ZrS_3, and HfS_3 have strong polarization dependence in such a way that intensity is at its maximum when the polarization direction is parallel to the anisotropic *b*-axis. This allows us to readily identify the Raman peaks that are representative of the vibrations along the *b*-axis direction. Interestingly, similar angle resolved studies on the novel $TiNbS_3$ TMTC alloy reveal that determination of anisotropy/crystalline direction is rather difficult possibly due to loss of anisotropy by randomization distribution of quasi-1D MX_6 chains by the presence of defects which are commonly found in 2D alloys and also due to the complex Raman tensor of TMTC alloys. Overall, the experimental and theoretical results establish non-destructive methods used to identify the direction of anisotropy in TMTCs and reveal their vibrational characteristics which are necessary to gain insight into potential applications that utilize direction dependent thermal response, optical polarization, and linear dichroism.

Introduction

Two-dimensional (2D) materials have gained massive attention in recent years due to the unique properties they obtain through strong quantum confinement effects.[1] Graphene's discovery[2] paved the way for many new classes of 2D materials such as the transition metal dichalcogenides (TMDCs) to be investigated. TMDCs (MoS_2, WS_2, $MoSe_2$, *etc.*) are structurally isotropic, layered materials that stack *via* weak van der Waals forces[3] and possess layer dependent optical and electronic properties which enable their versatile application in field emission,[4–6] transistors,[7,8] energy storage,[9] optoelectonics,[10] and sensing devices.[8,11–13] However, pseudo-one-dimensional (Pseudo-1D) materials are new classes of layered materials

where each layer displays strong in-plane anisotropy.[14–25] This unique feature distinguishes them from conventional 2D crystal structures, where atoms are arranged uniformly with isotropic material properties.[26] Examples of pseudo-1D materials include but are not limited to black phosphorus,[18,20] ReS_2[14,15,27] and $ReSe_2$[28,29] from the TMDCs, GaTe from the post-transition metal chalcogenides (PTMCs),[30–36] and more recently TiS_3 from the transition metal trichalcogenides (TMTCs).[22–24,37,38] The in-plane atoms of these materials arrange themselves in such a way that they form chain-like structures extending along a given lattice direction which leads to strong anisotropic behavior that offers additional advantages over isotropic 2D systems.[19–25]

In particular, recent theoretical studies on 2D TMTC TiS_3 have shown that these materials possess rather unique material properties including, high carrier mobility along anisotropic chain directions, the presence of a direct band gap in 2D form, highly polarized excitons, and linear polarization, which make them attractive candidates for device applications.[25] Overall, pseudo-1D TMTCs have the chemical formula MX_3 where M stands for the group IV transition metal atom and X is an element belonging to the chalcogen family (*e.g.* S, Se, or Te). The monoclinic unit cell of

[a]School for Engineering of Matter, Transport and Energy, Arizona State University, Tempe, Arizona 85287, USA. E-mail: sefaattin.tongay@asu.edu
*[b]Department of Physics, Izmir Institute of Technology, 35430 Izmir, Turkey*
[c]Department of Photonics, Izmir Institute of Technology, 35430 Izmir, Turkey
[d]LeRoy Eyring Center for Solid State Science, Arizona State University, Tempe, Arizona 85287, USA
[e]Department of Physics, Alliance College of Engineering and Design (ACED), Alliance University, Chandapura, Anekal, Bangalore, 562106 Karnataka, India

TMTCs has a $p2_{1/m}$ space group symmetry and contains 2 metal and 6 chalcogen atoms.[25] Within each unit cell, some M–X bond lengths are longer than others in one planar direction which leads to the formation of quasi-1D chain-like structures with a trigonal prismatic configuration as a result of in-plane dimerization.[23] Planar TMTC sheets are formed from rows of chains interacting with one another in an alternating manner as shown in the Fig. 1a. Unlike black phosphorus or ReS$_2$, the interactions between these chains are much weaker, which allows MX$_3$ materials to cleave in nano-ribbon shapes when exfoliated.[22–25,39,40] We call this chain length direction the b-axis direction which is also parallel to the preferential growth direction of the crystal. It is also important to note that TMTCs might not always cleave into nano-ribbons and that visual identification of the b-axis may not be reliable. Many of the properties of TMTCs are found to be quite more prominent along the b-axis compared to other crystalline orientations.[23,24] TiS$_3$ sheets exhibit a high electronic mobility of 80 cm^2 V^{-1} s^{-1} along the b-axis direction.[41] ZrS$_3$, with a bandgap of 1.8 eV, shows photoluminescence intensity variation dependent on its crystal direction relative to laser polarization.[22] HfS$_3$, under increasing strain, undergoes a transition from indirect to direct band gap with a direct gap of 2.2 eV.[42]

Despite their unique advantages over 2D systems, our understanding of fundamental vibrational properties of ultra-thin TMTC materials is still at its seminal stage. There is an urgent need for non-destructive optical techniques to correlate the direction of anisotropy with atomic vibrational (Raman) characteristics for quick identification of crystalline directions prior to other post-processing steps towards a variety of applications. As such, we aim to address the following fundamental questions involving TMTC materials: What is the origin of the most-prominent Raman peaks of Ti, Zr, and Hf based TMTCs? Do these materials all have similar vibrational characteristics (vibrational modes)? How can one correlate their Raman peaks to the chain direction of TMTCs? How is the anisotropic response of TMTCs influenced when they are alloyed? The latter question, in particular, is directly related to overall anisotropic properties and the degree of anisotropy since point defects, commonly found in alloy systems, are known to change the anisotropy in pseudo-1D systems like ReS$_2$ and ReSe$_2$.[17,43] Indeed, our studies reveal that anisotropy in the b-axis direction is largely lost in TMTC alloys due to the substantial amount of point defects present. Overall, this work employs angle-resolved Raman spectroscopy for the first time for multiple TMTC materials, and provides a fundamental understanding of their vibrational characteristics.
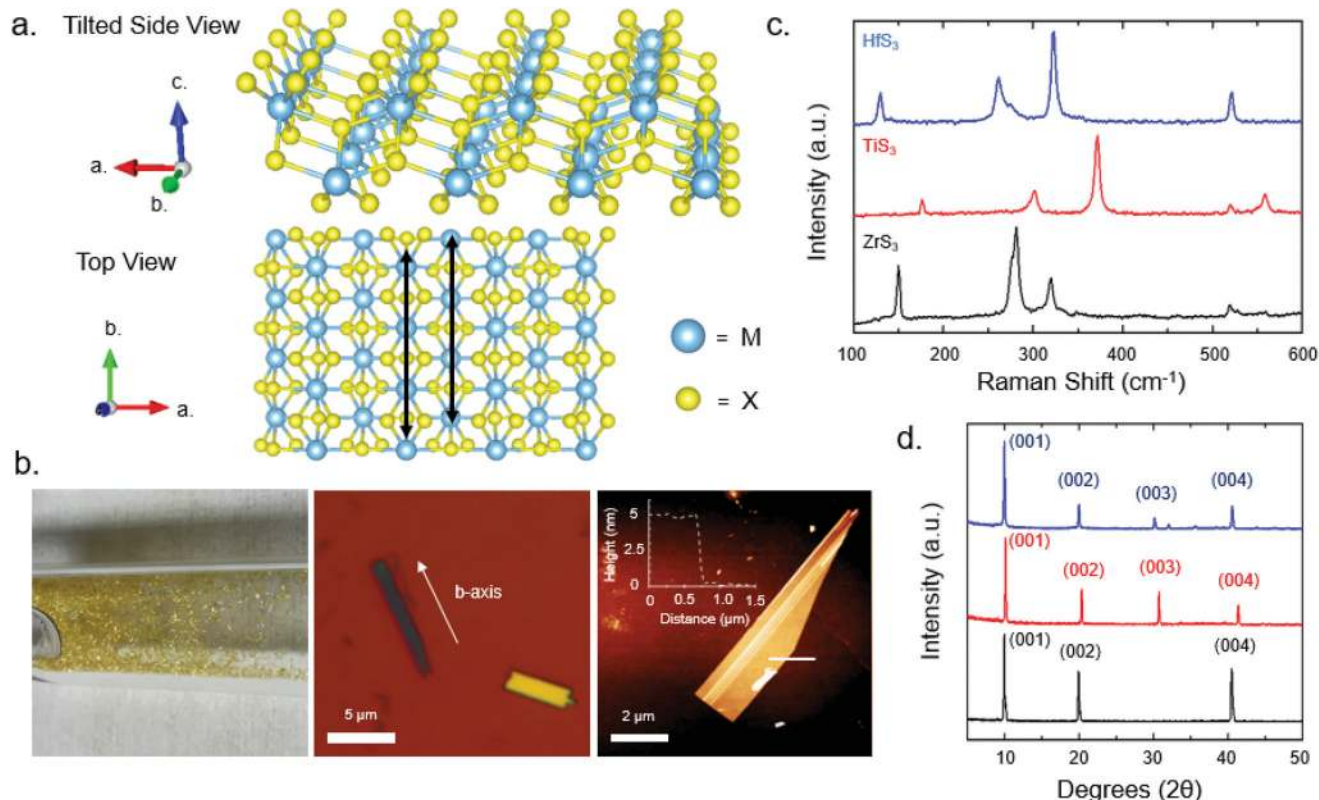
Fig. 1 (a) Tilted side view of a typical MX$_3$ crystal structure. A top view is shown with the black arrows indicating adjacent chain-like structures. The blue atoms represent the transition metals while the yellow atoms represent the chalcogen atoms. (b) Optical photograph of HfS$_3$ needles grown on the inner walls of a quartz ampoule, optical image of ZrS$_3$ flakes exfoliated onto SiO$_2$ substrates with the b-axis direction shown, and an AFM image of an exfoliated TiS$_3$ flake with thickness of ~5 nm. (c) Raman spectra obtained for TiS$_3$, ZrS$_3$, and HfS$_3$ bulk flakes using a 488 nm laser (d) powder X-ray diffraction peaks of TiS$_3$ (red), ZrS$_3$ (black), and HfS$_3$ (blue) bulk material.

Results and discussion

Synthesis and characterization

Explored trichalcogenides material systems, namely TiS_3, ZrS_3, and HfS_3, are not currently commercially available from standard vendors. In this work, we have synthesized these materials through chemical vapor transport methods using pelletized sulfur and elemental sheets of Ti, Zr, and Hf.[44] Typical growth process steps are detailed in the methods section but in general, the precursors were vacuum-sealed in quartz ampoules and placed into a two-zone tube furnace, heated to a temperature range of 520–650 °C. The bulk crystal growth spanned a period of 5 days and the furnace was cooled naturally to room temperature before the ampoule was removed from the furnace and opened. Trichalcogenide crystals that form on the inner walls of the quartz ampoule appear in a needle-like fashion due to their anisotropic structures (Fig. 1b). Mechanically exfoliated TiS_3, ZrS_3, and HfS_3 crystals on SiO_2/Si substrates with dimensions on the order of microns (Fig. 1b) are located through an optical microscope. Thin flakes with thicknesses less than 10 nm were visually identified through their violet contrast and confirmed using atomic force microscopy (AFM) (Fig. 1b).[45] The thin HfS_3 flake was continually damaged even under low laser power during the Raman measurements and the crystal was instead exfoliated onto bare silicon (111) in order to better dissipate the heating from the laser. Powder X-ray diffraction (XRD) was also performed on each of the bulk crystals to confirm their monoclinic crystal structures (Fig. 1d).

Vibrational characteristics

Unlike other 2D materials, such as TMDCs, the vibrational properties of trichalcogenides remain relatively unknown. Recent studies on TiS_3 by our team and others have identified the characteristic eigenmodes observed by the Raman spectrum, however it is currently unknown if similar conclusions can be drawn for other members of the trichalcogenides. To this end,

we have explored the vibrational properties of TMTC materials by using small displacement method[22,23] with forces obtained from density functional theory (DFT) calculations. The calculated phonon band dispersion for each TMTC containing 8 atoms in the primitive unit cell (Fig. 2a) has 3 acoustic branches and 21 optical branches. The Raman spectra for TiS_3 (Fig. 1c) shows four Raman active modes at 172, 299, 372, and 557 cm^{-1} as indicated by the blue, red, green, and orange labels respectively, in Fig. 2a.[24] Similarly, there are four modes at 151, 281, 320, and 528 cm^{-1} for ZrS_3 and four active modes found at 128, 260, 321, and 524 cm^{-1} for HfS_3, respectively. Experimentally determined Raman peaks match reasonably well with the theoretically calculated phonon dispersion. The peak seen at the 521 cm^{-1} position for all of the Raman spectra comes from the silicon substrate. No other 1st order Raman modes are observed beyond 600 cm^{-1}. Each mode corresponds to a particular atomic motion of a unit cell of atoms on the a–c plane (Fig. 2b). In this article, we will refer to these Raman active A_g modes from lowest to highest frequency as mode I, II, III, and IV respectively. We note that independent from the material type, the Raman peaks from low to high frequencies display fairly similar atomic motions. The directions of the eigenvectors for mode I (172, 151, and 128 cm^{-1} for TiS_3, ZrS_3, and HfS_3 respectively) show the sulfur and metal atoms within each chain with opposing vibrations. This out-of-plane motion extends along the trigonal prismatic chain in the b-axis direction. Because the vibrations of atoms within a chain stay in-phase, they are considered rigid vibrations.[23] Similarly, modes II and III also exhibit very similar out-of-plane atomic motions but involve the sulfur and metal atoms within each chain vibrating in opposing directions. TiS_3 in particular shows degenerate optical phonon branches in mode II demonstrated by Wu et al.[23] Interestingly, mode IV contains degenerate phonon branches and involves in-plane atomic vibration of sulfur atoms in pairs; therefore, mode IV can be referred to as in-plane or S–S diatomic oscillations.
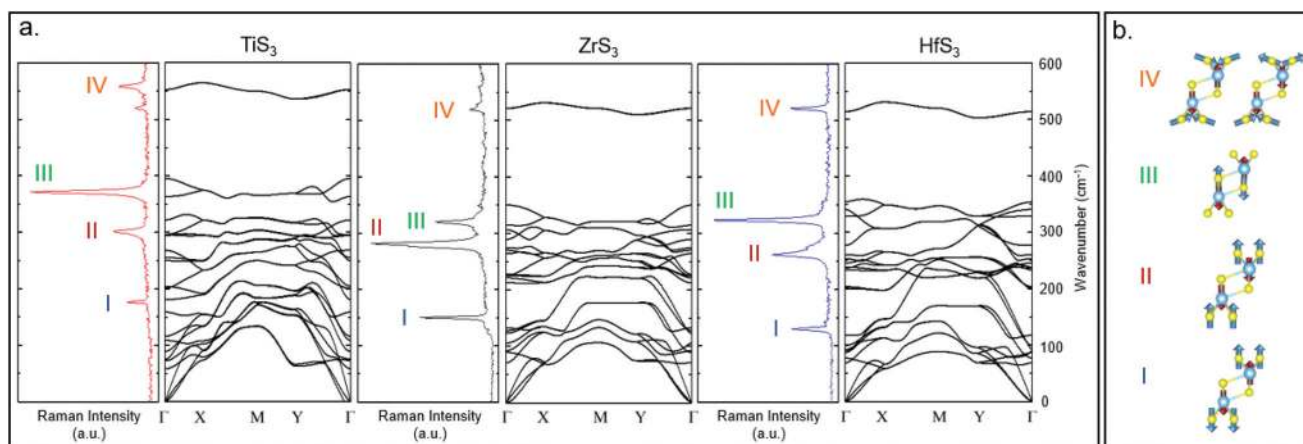
Fig. 2   (a) Phonon dispersion curves calculated using small displacement method for TiS_3, ZrS_3, and HfS_3 with colored labels indicating the Raman active mode that corresponds with a particular branch. (b) Atomic motions for each of the vibrational modes in (a) with eigenvectors that illustrate their direction of motion; the blue arrows indicate sulfur atom motion while the red arrows indicate the metal atom motion.

Anisotropy

In order to understand the polarization anisotropy of the MX_3 materials, angle-resolved Raman spectroscopy (operating under 488 nm excitation laser) was utilized as a quick and non-destructive optical method to probe this response. Here, we first focus on trichalcogenide flakes that measured in 50–100 nm in thickness (Fig. 3a) but similar results for ultra-thin samples that are thinner than 10 nm are also presented to test the consistency of Raman response for different thickness values. Flakes were aligned with the longer edge (*b*-axis) facing parallel to both the polarization direction of the incident laser excitation and the polarization detection direction of the Raman system. This orientation of the flake was defined as the

zero-degree position with theta being the angle between the *b*-axis and the polarization excitation/detection (inset in Fig. 3a). Polarization directions of the laser light were interchanged between normal and orthogonal to the detector with respect to the zero-degree position of the flake. Normal polarization refers to the excitation and detection directions arranged parallel to each other while orthogonal polarization is when these directions are offset by 90 degrees. Since the normal polarization response is much higher than that of orthogonal polarization, we only concentrate on the former to discuss the *b*-axis directions in this work.

As the theta angle between the *b*-axis and zero-degree position increased, the observed intensity for each Raman active peak shifted in magnitude with some modes being more sensi-
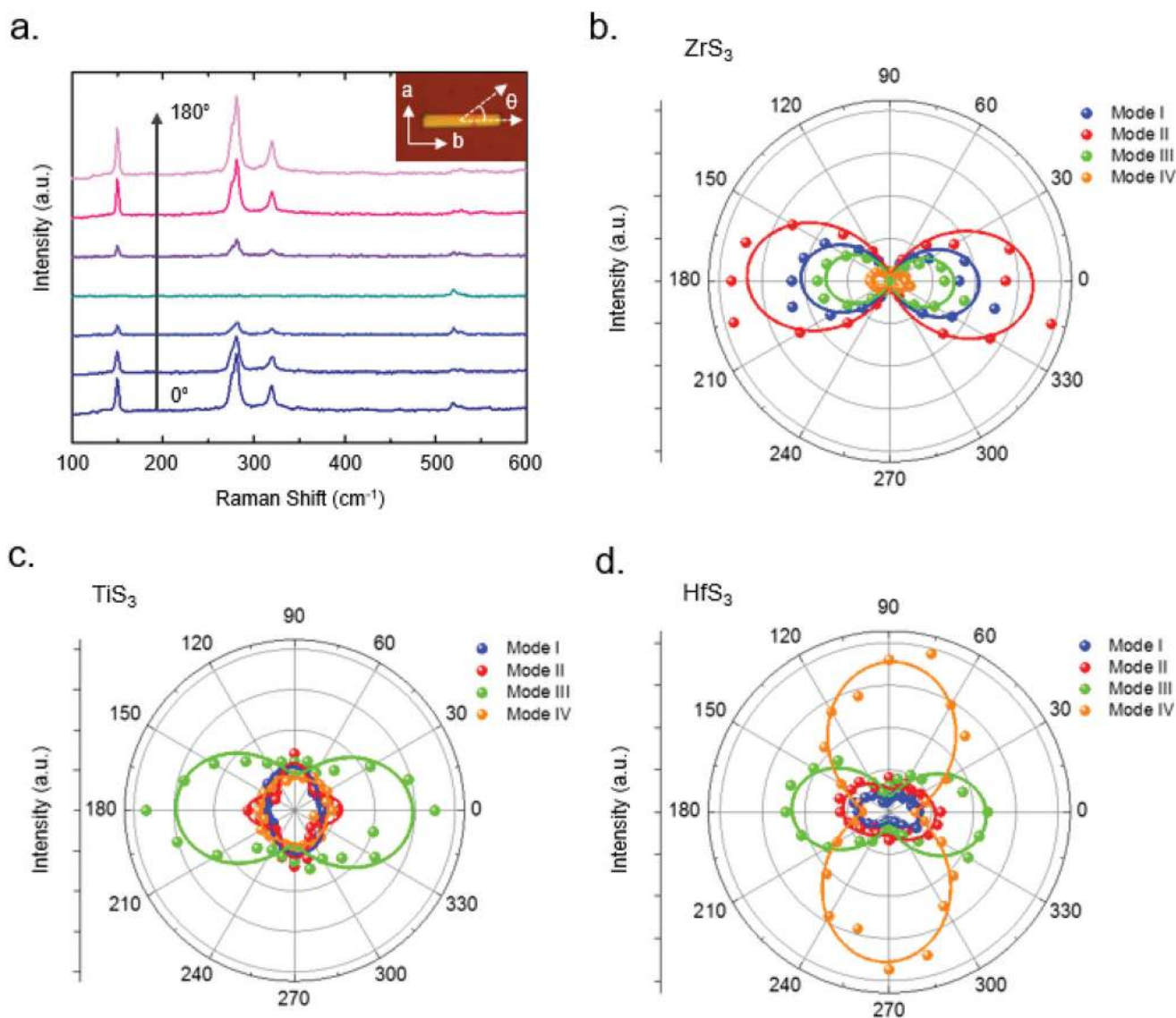
Fig. 3 (a) Raman spectra of ZrS_3 flake as a function of angle relative to the polarization direction and the *b*-axis. Plots are shown from 0 to 180° in 30° increments. Inset picture shows a ZrS_3 flake with crystal directions indicated and theta being the angle between the *b*-axis and polarization directions (b) polar plot for all ZrS_3 modes with mode III corresponding with 320 cm^{-1} (c) polar plot of all TiS_3 modes with mode III at 372 cm^{-1} (d) polar plot of all HfS_3 modes with mode III at 321 cm^{-1}.

tive than others. A closer look at the Raman spectrum of ZrS_3 exfoliated flakes show that variety of Raman modes changes in intensity at different increments of theta (Fig. 3a). Using the intensity values of select Raman peaks, a polar plot is generated for a full 360-degree rotation which illustrates the peak intensity of a particular mode as a function of angle theta with respect to the zero-degree position. For flakes with their b-axis aligned parallel with the excitation polarization at 0° and 180°, the intensity of certain modes reach their maximum value while their lowest values are found at theta values of 90° and 270°. This behavior is depicted in the form of a two-lobed plot where the lobes are aligned parallel with the zero-degree position. In general, modes I–III for TiS_3, ZrS_3, and HfS_3 show some level anisotropy when polarized by the laser excitation which can be attributed to their unique out-of-plane metal–sulfur vibrations. Mode IV is an exception since the atomic vibrations only involve in-plane oscillations of sulfur atoms which do not contribute to the overall anisotropic response of the materials. In selecting representative peaks for the identification of crystalline directions for each of these materials, we find that not all modes across the three materials behave in similar manner. The subtle variations between the atomic spacing and bond lengths for TMTCs can attribute to slightly different vibrational motions in each mode.

For the Raman-active peaks in TiS_3, the 372 cm^{-1} peak corresponding to mode III was the most prominent of the 4 peaks and quite sensitive to changes in peak intensity at different angles. The TiS_3 polar plot shows a two-lobed shape for mode III with the b-axis of the flake aligned parallel to the zero-degree position (Fig. 3c). However, this behavior is not seen in the remaining TiS_3 Raman modes. ZrS_3, on the other hand, shows the same two-lobed shape along the zero-degree position for all modes with mode II exhibiting the strongest response and mode IV the weakest. Modes I–III for HfS_3 also display this two-lobed plot along the zero-degree position. In contrast to other peaks, mode IV generally displays rather weak polarization dependence, thus does not provide an adequate

signal to be used for a determination of crystal direction. Based on our vibrational analysis results in Fig. 2, this is possibly due to the fact that mode IV mainly involves S–S atomic vibration modes which does not represent the crystalline anisotropy direction or the crystal symmetry of the material itself. Mode IV for HfS_3 is an exception to this by showing strong variations in Raman intensity at different theta with a resulting two-lobed plot offset from the zero-degree position by 90 degrees. While other low frequency modes can also be used for identification of the crystalline axis, mode III is the most reliable as each polar plot shows the same anisotropic behavior along the b-axis and is present in each TMTC material.

Thickness response

We next performed similar studies on ultra-thin flakes ($t <$ 10 nm) to determine if the same trends can be seen in and similar conclusion can be drawn for both bulk and thin flakes. Angle-resolved Raman spectroscopy was employed for flake thicknesses below 10 nm with the exception of the HfS_3 flake at a thickness of ~20 nm. Atomic force microscopy in tapping mode was utilized to confirm the thickness and morphology of these thin flakes. The polar plots for the thin flakes also illustrated the same two-lobed shapes that lie parallel to the zero-degree position. Again, only mode III plots were shown due to their common anisotropic behavior between each of the TMTC systems. These measurements yielded similar results to thicker flakes (Fig. 4a). These plots do not change in shape or orientation for thin flakes. Even for MX_3 materials at a lower thickness, angle-resolved Raman spectroscopy remains a consistent method for determining the b-axis of the material.

Effects of alloying on the anisotropy

While we have demonstrated that TMTC materials polarize strongly along the b-axis through optical methods, TMTC alloy materials are anticipated to be more challenging due to the presence of extended defects which are known to randomize the chain direction in quasi-1D materials as shown in ReS_2
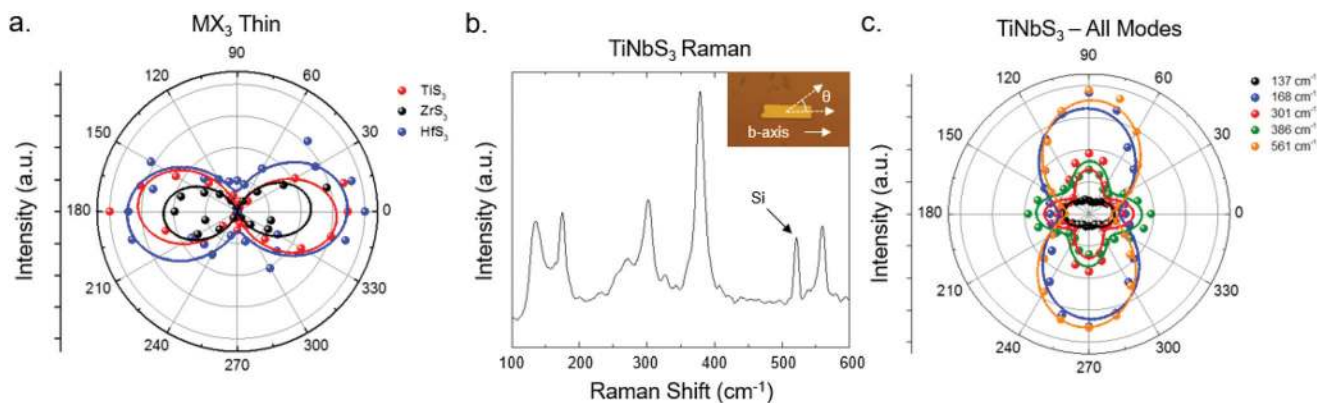

Fig. 4 (a) Polar plot of mode III at 372 (red), 320 (black), and 321 cm^{-1} (blue) that correspond to thin TiS_3, ZrS_3, and HfS_3 flakes respectively. (b) Raman spectra of $TiNbS_3$ with the silicon peak indicated. Inset image shows a $TiNbS_3$ flake with the b-axis indicated and theta being the angle between the polarization direction and the b-axis (c) polar plot of the 5 Raman modes shown for the alloy material, $TiNbS_3$.

and ReSe$_2$.[17,43] In order to test the applicability of angle-resolved Raman spectroscopy technique for determining the crystalline axis of alloys, we have synthesized TiNbS$_3$ crystals for the first time and mechanically exfoliated them to few layer nano-ribbons. The synthesis procedure is similar to that of the other MX$_3$ materials with the ratio of Ti and Nb kept 1 : 1. Raman spectroscopy studies show that the TMTC alloy is crystalline as evidenced by prominent and sharp Raman peaks (FWHM ~ 5–6 cm^{-1}) located at 137, 168, 301, 386, and 561 cm^{-1} (Fig. 4b). Angle-resolved Raman spectroscopy polar plots (Fig. 4c) for these prominent peaks displays a weak 2-lobed plot that lies along the zero-degree position and two strong two-lobed shapes with maximums at 90 and 270 degrees. Additionally, there are two symmetric 4-lobed plots that show maximum intensity at 0, 90, 180, and 270 degrees. While some anisotropic effects can be seen with the given plots, there is no clear indication which modes correlate to the *b*-axis direction based on our prior definitions. Such complicated polar plots are likely be related to the more complex Raman tensor of trichalcogenides alloys that prevents us to reach a simple conclusion as well as the presence of variety of point defects commonly found in alloyed materials which are known to randomize the chain (anisotropy) direction in pseudo-1D material systems. Thus, angle resolved Raman spectroscopy measurements on TMTCs alloys requires extra attention for proper analysis to identify the anisotropy direction, and more theoretical studies are required to shed light on their fundamental Raman characteristics.

Conclusion

To summarize, we investigated the polarization dependent vibrational properties of various TMTC materials (TiS$_3$, ZrS$_3$, and HfS$_3$) as well as a novel TMTC alloy (TiNbS$_3$) thorough density functional theory calculations, atomic force microscopy, and angle-resolved Raman spectroscopy. Our results provide an important guideline for a quick and non-destructive optical determination of anisotropic structural properties of TMTCs. In particular, these results show that the strong out-of-plane motion of inner atoms (mode III) for TiS$_3$, ZrS$_3$, and HfS$_3$ align parallel to the quasi-1D chains that extend along the direction of the *b*-axis. Results also show that the anisotropy of the Raman peak intensity is preserved and insensitive to the thickness of TMTCs. Therefore, this methodology can be broadly applied to both bulk and monolayers. Lastly, our studies on TMTC alloys show that optical techniques that probe atomic vibrations produce insufficient indicators of structural anisotropy due to the presence of point defects. This work not only provides necessary guidelines for identifying the crystalline directions and anisotropy of TMTCs, but also elucidates the vibrational properties of pseudo-1D trichalcogenides in attempt to unify their vibrational characteristics which is necessary for further understanding of the thermal, optical, and electrical behavior of TMTCs and exploring their applications in photonic and optoelectronics.

Experimental

Crystal growth and characterization

Each MX$_3$ material was grown by chemical vapor transport (CVT) method using Ti, Zr, and Hf elemental sheets and excess sulfur pellets kept at a stoichiometric 1 : 3 ratio. A total amount of 1 g of the precursor materials was placed into one end of a quartz tube and vacuum-sealed at around 10^{-6} Torr. The ampoule was loaded into a two-zone furnace which was heated up to a growth temperature of 520 °C for TiS$_3$ and 650 °C for both ZrS$_3$ and HfS$_3$. The heating rate was 2 °C min^{-1} in order to prevent any highly destructive exothermic reactions from taking place. A temperature gradient of 100 °C within 20 cm was maintained during the growth. The growth for each material took place over the course of 5 days and the quartz tube was cooled down to room temperature naturally once the growth was completed. A band saw was used to open the sealed ampoules to remove the crystals that have grown along the inner walls of the ampoule. TiNbS$_3$ was synthesized in a similar manner as TiS$_3$ with the Nb and Ti precursors kept at 1 : 1 stoichiometric ratio. The growth temperature for this alloy was 550 °C during a growth period of 3 days. The crystallinity of the CVT-grown samples was examined through powder X-ray diffraction (XRD) technique (Siemens D5000) using Cu Kα irradiation (λ = 1.54 Å). Typically, a small piece of sample was mounted onto a zero-background plate and the 2θ angle ranging from 5 to 65 degrees. Atomic force microscopy (AFM) was conducted using the Dimension Multimode 8 under tapping mode. Depending on the size of the area of interest, the resolution was set at 256 × 256, and the scanning rate was typically set to at 1.0 Hz.

Computational methodology

The monolayer MX$_3$ (M = Ti, Zr, Hf and X = S) crystal structures were calculated using VASP code[46–48] which is based on density functional theory (DFT). The Perdew–Burke–Ernzerhof (PBE) form of the generalized gradient approximation (GGA)[49] was adopted to describe electron exchange and correlation. The kinetic energy cut-off of the plane-wave basis set was 500 eV. Brillouin Zone integration was performed using a 20 × 15 × 1 Γ-centered mesh for the primitive unit cell. The total energy difference between the sequential steps in each iterations taken 10^{-6} eV as convergence criterion. Gaussian smearing of 0.05 eV was used and the pressures on the unit cell were decreased to a value less than 1.0 kB in all three dimensions. The vibrational properties were calculated for 128-atom-supercell using the small displacement method.[50]

Angle-resolved Raman spectroscopy

The Raman spectrometer used was a Renishaw InVia system with a 488 nm laser focused through a 100× objective lens. The substrates were placed on a microscope stage containing a rotating disk. The flakes were mechanically exfoliated onto SiO$_2$/Si substrates and the visibly longer edge was aligned parallel with the polarization direction of the incident laser light and referenced as the zero-degree position. Raman measure-

ments started at the zero-degree position and rotated by 15 degree increments for each additional measurement until a full rotation was completed. The intensity of each Raman-active mode was plotted as a function of rotation angle with respect to the zero-degree position. Each polar plot was generated using OriginLab software.

Acknowledgements

References

1 Q. Wang, K. Kalantar-Zadeh, A. Kis, J. Coleman and M. Strano, *Nat. Nanotechnol.*, 2012, **7**, 699–712.

2 A. Geim, *Science*, 2009, **324**, 1530–1534.

3 H. S. S. Ramakrishna Matte, A. Gomathi, A. K. Manna, D. J. Late, R. Datta, S. K. Pati and C. N. R. Rao, *Angew. Chem., Int. Ed.*, 2010, **122**, 4153–4156.

4 R. Kashid, D. Late, S. Chou, Y. Huang, M. De, D. Joag, M. More and V. Dravid, *Small*, 2013, **9**, 2730–2734.

5 S. Suryawanshi, M. More and D. Late, *RSC Adv.*, 2016, **6**, 2730–2734.

6 C. Rout, P. Joshi, R. Kashid, D. Joag, M. More, A. Simbeck, M. Washington, S. Nayak and D. Late, *Sci. Rep.*, 2013, **3**, 3282.

7 D. Late, B. Liu, R. Matte, V. Dravid and C. N. R. Rao, *ACS Nano*, 2012, **6**, 5635–5641.

8 D. Late, Y.-K. Huang, B. Liu, J. Acharya, S. Shirodkar, J. Luo, A. Yan, D. Charles, U. Waghmare, V. Dravid and C. N. R. Rao, *ACS Nano*, 2013, **7**, 4879–4891.

9 D. Chakravarty, P. Kumar, V. Ugale and D. Late, *Eur. J. Inorg. Chem.*, 2015, **9**, 1598–1603.

10 D. Late, *Appl. Mater. Today*, 2016, **5**, 98–102.

11 D. Late, T. Doneux and M. Bougouma, *Appl. Phys. Lett.*, 2014, **105**, 233103.

12 D. Late, *Microporous Mesoporous Mater.*, 2016, **225**, 494–503.

13 D. Late, R. Kanawade, P. Kannan and C. Rout, *Sens. Lett.*, 2016, **14**, 1249–1254.

14 S. Tongay, H. Sahin, C. Ko, A. Luce, W. Fan, K. Liu, J. Zhou, Y.-S. Huang, C.-H. Ho, J. Yan, F. Ogletree, S. Aloni, J. Ji, S. Li, J. Li, F. M. Peeters and J. Wu, *Nat. Commun.*, 2014, **5**, 3252.

15 D. Chenet, B. Aslan, P. Huang, C. Fan, A. van der Zande, T. Heinz and J. Hone, *Nano Lett.*, 2015, **15**, 5667–5672.

16 L. Hart, S. Dale, S. Hoye, J. Webb and D. Wolverson, *Nano Lett.*, 2016, **16**, 1381–1386.

17 K. Wu, B. Chen, S. Yang, G. Wang, W. Kong, H. Cai, T. Aoki, E. Soignard, X. Marie, A. Yano, A. Suslu, B. Urbaszek and S. Tongay, *Nano Lett.*, 2016, **16**, 5888–5894.

18 H. Liu, A. Neal, Z. Zhu, Z. Luo, X. Xu, D. Tománek and P. Ye, *ACS Nano*, 2014, **8**, 4033–4041.

19 S. Lee, F. Yang, J. Suh, S. Yang, Y. Lee, G. Li, H. Choe, A. Suslu, Y. Chen and C. Ko, *Nat. Commun.*, 2015, **6**, 8573.

20 X. Ling, H. Wang, S. Huang, F. Xia and M. Dresselhaus, *Proc. Natl. Acad. Sci. U. S. A.*, 2015, **112**, 4523–4530.

21 X. Wang, A. Jones, K. Seyler, V. Tran, Y. Jia, H. Zhao, H. Wang, L. Yang, X. Xu and F. Xia, *Nat. Nanotechnol.*, 2015, **10**, 517–521.

22 A. Pant, E. Torun, B. Chen, S. Bhat, X. Fan, K. Wu, D. Wright, F. Peeters, E. Soignard, H. Sahin and S. Tongay, *Nanoscale*, 2016, **8**, 16259–16265.

23 K. Wu, E. Torun, H. Sahin, B. Chen, X. Fan, A. Pant, D. Wright, T. Aoki, F. Peeters, E. Soignard and S. Tongay, *Nat. Commun.*, 2016, **7**, 12952.

24 J. Island, R. Biele, M. Barawi, J. Clamagirand, J. Ares, C. Sánchez, H. van der Zant, I. Ferrer, R. D'Agosta and A. Castellanos-Gomez, *Sci. Rep.*, 2016, **6**, 22214.

25 J. Dai and X. Zeng, *Angew. Chem., Int. Ed.*, 2015, **127**, 7682–7686.

26 M. Chhowalla, H. Shin, G. Eda, L.-J. Li, K. Loh and H. Zhang, *Nat. Chem.*, 2013, **5**, 263–275.

27 F. Liu, S. Zheng, X. He, A. Chaturvedi, J. He, W. Chow, T. Mion, X. Wang, J. Zhou, Q. Fu, H. Fan, B. Tay, L. Song, R. He, C. Kloc, P. Ajayan and Z. Liu, *Adv. Funct. Mater.*, 2016, **26**, 1169–1177.

28 S. Yang, S. Tongay, Y. Li, Q. Yue, J.-B. Xia, S.-S. Li, J. Li and S.-H. Wei, *Nanoscale*, 2014, **6**, 7226–7231.

29 S. Yang, S. Tongay, Q. Yue, Y. Li, B. Li and F. Lu, *Sci. Rep.*, 2014, **4**, 5442.

30 O. A. Balitskii, B. Jaeckel and W. Jaegermann, *Phys. Lett. A*, 2008, **372**, 3303–3306.

31 H. Cai, E. Soignard, C. Ataca, B. Chen, C. Ko, T. Aoki, A. Pant, X. Meng, S. Yang, J. Grossman, F. Ogletree and S. Tongay, *Adv. Mater.*, 2016, **28**, 7375–7382.

32 H. Cai, J. Kang, H. Sahin, B. Chen, A. Suslu and K. Wu, *Nanotechnology*, 2016, **27**, 065203.

33 J. Fonseca, S. Tongay, M. Topsakal, A. Chew, A. Lin, C. Ko, A. Luce, A. Salleo, J. Wu and O. Dubon, *Adv. Mater.*, 2016, **28**, 6465–6470.

34 S. Huang, Y. Tatsumi, X. Ling, H. Guo, Z. Wang, G. Watson, A. Puretzky, D. Geohegan, J. Kong, J. Li, T. Yang, R. Saito and M. Dresselhaus, *ACS Nano*, 2016, **10**, 8964–8972.

35 S. Yang, C. Wang, C. Ataca, Y. Li, H. Chen, H. Cai, A. Suslu, J. Grossman, C. Jiang, Q. Liu and S. Tongay, *ACS Appl. Mater. Interfaces*, 2016, **8**, 2533–2539.

36 Q. Zhao, T. Wang, Y. Miao, F. Ma, Y. Xie, X. Ma, Y. Gu, J. Li, J. He, B. Chen, S. Xi, L. Xu, H. Zhen, Z. Yin, J. Li, J. Ren and W. Jie, *Phys. Chem. Chem. Phys.*, 2016, **18**, 18719–18726.

37 A. Lipatov, P. Wilson, M. Shekhirev, J. Teeter, R. Netusil and A. Sinitskii, *Nanoscale*, 2015, **7**, 12291–12296.

38 A. Pawbake, J. Island, E. Flores, J. Ares, C. Sanchez, I. Ferrer, S. Jadkar, H. van der Zant, A. Castellanos-Gomez and D. Late, *ACS Appl. Mater. Interfaces*, 2015, **7**, 24185–24190.

39 J. Kang, H. Sahin, D. Ozaydin, T. Senger and F. Peeters, *Phys. Rev. B: Condens. Matter*, 2015, **92**, 075413.

40 Y. Aierken, D. Çakır and F. Peeters, *Phys. Chem. Chem. Phys.*, 2016, **18**, 14434–14441.

41 J. Island, M. Barawi, R. Biele, A. Almazán, J. Clamagirand, J. Ares, C. Sánchez, H. van der Zant, J. Álvarez, R. D'Agosta, I. Ferrer and A. Castellanos-Gomez, *Adv. Mater.*, 2015, **27**, 2595–2601.

42 M. Li, J. Dai and X. Zeng, *Nanoscale*, 2015, **7**, 15385–15391.

43 Y.-C. Lin, H.-P. Komsa, C.-H. Yeh, T. Björkman, Z.-Y. Liang, C.-H. Ho, Y.-S. Huang, P.-W. Chiu, A. Krasheninnikov and K. Suenaga, *ACS Nano*, 2015, **9**, 11249–11257.

44 S. Furuseth, L. Brattas and A. Kjekshus, *Acta Chem. Scand.*, 1975, **29**, 623.

45 D. Late, B. Liu, R. Matte, C. N. R. Rao and V. Dravid, *Adv. Funct. Mater.*, 2012, **22**, 1894–1905.

46 G. Kresse and J. Hafner, *Phys. Rev. B: Condens. Matter*, 1993, **47**, 558–561.

47 G. Kresse and D. Joubert, *Phys. Rev. B: Condens. Matter*, 1999, **59**, 1758–1775.

48 G. Kresse and J. Furthmüller, *Phys. Rev. B: Condens. Matter*, 1996, **54**, 11169–11186.

49 J. P. Perdew, K. Burke and M. Ernzerhof, *Phys. Rev. Lett.*, 1996, **77**, 3865–3868.

50 D. Alfè, *Comput. Phys. Commun.*, 2009, **180**, 2622–2633.